



Article

In Situ Growth of CdZnS Nanoparticles@Ti₃C₂T_x MXene Nanosheet Heterojunctions for Boosted Visible-Light-Driven Photocatalytic Hydrogen Evolution

Zelin Li ^{1,2}, Yang Zhao ^{1,2}, Qinglin Deng ^{1,2,*} , Xuhui Zhu ^{1,2}, Yipeng Tan ^{1,2}, Ziwen Feng ^{1,2}, Hao Ji ^{1,2}, Shan Zhang ^{1,2,*} and Lingmin Yao ^{1,2}

¹ School of Physics and Materials Science, Guangzhou University, Guangzhou 510006, China; zl-li@foxmail.com (Z.L.); zy843795537@163.com (Y.Z.); zxx2674091377@foxmail.com (X.Z.); a1693433393@outlook.com (Y.T.); ziwenfeng@foxmail.com (Z.F.); jihao0114@foxmail.com (H.J.); lingminyao@gzhu.edu.cn (L.Y.)

² Research Center for Advanced Information Materials (CAIM), Huangpu Research & Graduate School of Guangzhou University, Guangzhou 510555, China

* Correspondence: qldeng@gzhu.edu.cn (Q.D.); szhang@gzhu.edu.cn (S.Z.)

Abstract: Using natural light energy to convert water into hydrogen is of great significance to solving energy shortages and environmental pollution. Due to the rapid recombination of photogenerated carriers after separation, the efficiency of photocatalytic hydrogen production using photocatalysts is usually very low. Here, efficient CdZnS nanoparticles@Ti₃C₂T_x MXene nanosheet heterojunction photocatalysts have been successfully prepared by a facile in situ growth strategy. Since the CdZnS nanoparticles uniformly covered the Ti₃C₂T_x MXene nanosheets, the agglomeration phenomenon of CdZnS nanoparticles could be effectively inhibited, accompanied by increased Schottky barrier sites and an enhanced migration rate of photogenerated carriers. The utilization efficiency of light energy can be improved by inhibiting the recombination of photogenerated electron-hole pairs. As a result, under the visible-light-driven photocatalytic experiments, this composite achieved a high hydrogen evolution rate of 47.1 mmol h⁻¹ g⁻¹, which is much higher than pristine CdZnS and MXene. The boosted photocatalytic performances can be attributed to the formed heterojunction of CdZnS nanoparticles and Ti₃C₂T_x MXene nanosheets, as well as the weakened agglomeration effects.

Keywords: CdZnS; MXene; photocatalyst; heterojunction; hydrogen evolution



Citation: Li, Z.; Zhao, Y.; Deng, Q.; Zhu, X.; Tan, Y.; Feng, Z.; Ji, H.; Zhang, S.; Yao, L. In Situ Growth of CdZnS Nanoparticles@Ti₃C₂T_x MXene Nanosheet Heterojunctions for Boosted Visible-Light-Driven Photocatalytic Hydrogen Evolution. *Nanomaterials* **2023**, *13*, 2261. <https://doi.org/10.3390/nano13152261>

Academic Editor: Francesc Viñes Solana

Received: 13 July 2023

Revised: 2 August 2023

Accepted: 4 August 2023

Published: 6 August 2023



Copyright: © 2023 by the authors. Licensee MDPI, Basel, Switzerland. This article is an open access article distributed under the terms and conditions of the Creative Commons Attribution (CC BY) license (<https://creativecommons.org/licenses/by/4.0/>).

1. Introduction

Energy shortages and environmental pollution are the main problems facing the world today [1,2]. Hydrogen, a clean and carbon-free natural energy source with a high energy density, can aid in the better resolution of energy and environmental issues [3–5]. Currently, hydrogen is used in many fields, such as the oil industry, the new energy industry, and so on. As the demand for hydrogen continues to increase, the scientific community is also exploring ways to increase hydrogen production [6–8]. Since Fujishima and Honda discovered the phenomenon of photocatalytic water splitting in 1972 [9], scientists have been working on this technology. Photocatalytic hydrogen production, as a green and pollution-free technology that can convert solar energy into hydrogen energy, has now become one of the most promising research directions.

In the past decade, metal sulfides have been widely employed in various fields, such as optical imaging and energy storage applications [10–12], due to their excellent electronic, optical, and semiconductor properties. Transition metal sulfides, such as WS₂, MoS₂, ZnS, and CdS, are widely cited in the field of photocatalysis due to their suitable band gaps [13]. Ganapathy et al. [14] prepared amorphous SrTiO₃-crystalline PbS heterojunctions that exhibited a hydrogen production performance of 5.9 mmol h⁻¹ g⁻¹ under ultraviolet light

irradiation. Zhuge et al. [15] deposited molybdenum disulfide onto cadmium sulfide quantum dots, promoting charge separation and achieving a photocatalyst with hydrogen production performance as high as $13.13 \text{ mmol h}^{-1} \text{ g}^{-1}$. Among them, CdS exhibits prominent performance [16]. However, CdS suffers from poor stability and is associated with certain toxicities [17]. To overcome these issues, cadmium sulfide is typically coupled with other materials to form heterojunctions, aiming to achieve enhanced photocatalytic activity and improved photostability [18]. Zinc sulfide has a wide band gap and a similar structure to cadmium sulfide. Zinc sulfide and cadmium sulfide can form an infinitely miscible solid solution of $\text{Cd}_{1-x}\text{Zn}_x\text{S}$ [19–22]. The band gap of $\text{Cd}_{1-x}\text{Zn}_x\text{S}$ can be adjusted by controlling the ratio of zinc to cadmium in the range of 2.4–3.6 eV to achieve better photocatalytic stability and hydrogen production performance [23–25]. According to existing reports, when the ratio of zinc to cadmium is 1:1 (CdZnS, abbreviated as CZS), it has the best photocatalytic activity [23,26,27]. Moreover, the photocorrosion caused by the accumulation of photogenerated pores on the surface of single-transition metal sulfide and the recombination of photogenerated electron holes are the two main problems that affect the photocatalytic performance of CZS. At present, there are several mainstream improvement strategies, for example, loading a co-catalyst, constructing a heterojunction, coupling with nano-carbon, constructing a Z-scheme system, and so on [28]. One of the most effective strategies is to use precious metals (such as Pt, Au, etc.) as supported catalysts to facilitate the separation of photogenerated electron holes. The addition of metals with higher work functions and excellent conductivity can induce surface plasmon resonance (SPR) effects and Schottky barriers. This improves the dynamics of charge carriers through spatial confinement of electrons and accelerated migration for redox reactions [29]. However, due to the high price and low reserves, this strategy cannot be widely used; thus, a new co-catalyst is urgently needed [30–32].

Mxene is a two-dimensional material with the general form $\text{M}_{n+1}\text{X}_n\text{T}_x$, where M, X, and T represent the transition metal, C or N, and the surface ends involve -OH, -O and -F, respectively [28,33]. Among them, $\text{Ti}_3\text{C}_2\text{T}_x$ is one of the most promising materials, which has abundant hydrophilic functional groups, good conductivity, and optical response ability, as well as the advantages of enhanced carrier separation [34–36]. Moreover, due to its metallic nature, it can potentially form a Schottky barrier with semiconductor photocatalysts, thereby capturing electrons and playing a significant role in suppressing the recombination of photogenerated electrons. $\text{Ti}_3\text{C}_2\text{T}_x$ can increase the surface-active sites, which is more conducive to improving the hydrogen production performance of CZS [37–39]. Additionally, the layered structure of $\text{Ti}_3\text{C}_2\text{T}_x$ can be tailored into 2D or 3D morphologies, as needed, maximizing the utilization of light energy [29]. Based on the above characteristics, scholars have carried out a lot of research on $\text{Ti}_3\text{C}_2\text{T}_x$ as a co-catalyst. Yin et al. [27] in situ synthesized titanium dioxide nanoparticles on a Ti_3C_2 matrix and then hydrothermally formed Z-scheme $\text{TiO}_2@/\text{Ti}_3\text{C}_2/\text{Cd}_{0.5}\text{Zn}_{0.5}\text{S}$ (TO/CZS) multi-structure nanocomposites. The obtained photocatalyst has a higher degradation rate. Chen et al. [40] prepared a two-dimensional cadmium sulfide nanosheet composite $\text{Ti}_3\text{C}_2\text{T}_x$ photocatalyst with a higher photocatalytic activity. Tao et al. [28] reported the highest hydrogen evolution performance of $\text{CZS}@/\text{Ti}_3\text{C}_2\text{T}_x$ materials synthesized via a hydrothermal method, reaching $29.3 \text{ mmol h}^{-1} \text{ g}^{-1}$. Zhong et al. [35] synthesized $\text{CZS}/\text{Ti}_3\text{C}_2\text{A}_{40}$ with a maximum hydrogen evolution performance of $13.44 \text{ mmol h}^{-1} \text{ g}^{-1}$. A large number of studies have shown that $\text{Ti}_3\text{C}_2\text{T}_x$ as a co-catalyst can improve the efficiency of carrier migration and accelerate the transfer of charge. Moreover, the combination of zinc cadmium sulfide and $\text{Ti}_3\text{C}_2\text{T}_x$ not only improves the photocatalytic activity of CZS, but also alleviates the photocorrosion of CZS to some extent [41].

Due to the internal electric field generated by the heterojunction generated at the interface between the metal and the semiconductor, it can play a crucial role in promoting the separation of photocurrent-carrying electrons and improving the migration efficiency [42–44]. Inspired by this, we successfully constructed the heterojunction composite $\text{CZS}/\text{Ti}_3\text{C}_2\text{T}_x$ by a hydrothermal in-situ growth and assembly method in this work. The

negative charge of $\text{Ti}_3\text{C}_2\text{T}_x$ causes electrostatic adsorption, so cadmium and zinc ions could be tightly attached to $\text{Ti}_3\text{C}_2\text{T}_x$, which effectively inhibited the agglomeration of CZS nanoparticles. In this way, the efficient separation and utilization of electrons and holes can be realized. As a result, a kind of photocatalyst with more efficient hydrogen production performance can be obtained.

2. Materials and Methods

2.1. Materials

Chemicals (all analytical grade) were purchased from Aladdin Biochemical Technology Co., Ltd. (Shanghai, China) and used without further purification. These included zinc acetate dehydrate ($\text{Zn}(\text{OCOCH}_3)_2 \cdot 2\text{H}_2\text{O}$), cadmium acetate dehydrate ($\text{Cd}(\text{OCOCH}_3)_2 \cdot 2\text{H}_2\text{O}$), thioacetamide (TAA), sodium hydroxide (NaOH), sodium sulfide (Na_2S), and sodium sulfite (Na_2SO_3). $\text{Ti}_3\text{C}_2\text{T}_x$ was purchased from Xianfeng Nanomaterials Technology Co., Ltd. (Nanjing, China).

2.2. Synthesis of Photocatalysts

The CdZnS/ $\text{Ti}_3\text{C}_2\text{T}_x$ photocatalyst was synthesized by the method shown in Figure 1. Solution A: 2 mmol of cadmium acetate hydrate and 2 mmol of zinc acetate hydrate were dissolved in 4 mL of deionized water, and then an appropriate amount of $\text{Ti}_3\text{C}_2\text{T}_x$ was added to the above solution. Finally, the mixture was stirred for 1 h. Solution B: 5 mmol of thioacetamide (TAA) was added to 4 mL of deionized water, then dissolved by stirring. Solution C: 8 mmol NaOH was dissolved in 2 mL of deionized water. In a typical synthesis, Solution B was added dropwise to solution A and stirred for about 1 h. Then, 2 mL of 4 mol L^{-1} NaOH aqueous solution was added, drop by drop, in the stirred state after stirring for another hour. The mixture was hydrothermally treated at 180°C for 24 h. In this work, CdZnS samples with different ratios of $\text{Ti}_3\text{C}_2\text{T}_x$ were named CZS-1, CZS-2, CZS-2.5, CZS-3, and CZS-5, where the numbers represent the mass percentage of added $\text{Ti}_3\text{C}_2\text{T}_x$ (1%, 2%, 2.5%, 3%, and 5%). The preparation process of the original CZS is similar to that of the CZS@ $\text{Ti}_3\text{C}_2\text{T}_x$ composite photocatalyst, with the difference being the absence of $\text{Ti}_3\text{C}_2\text{T}_x$ in the precursor solution of the original CZS.

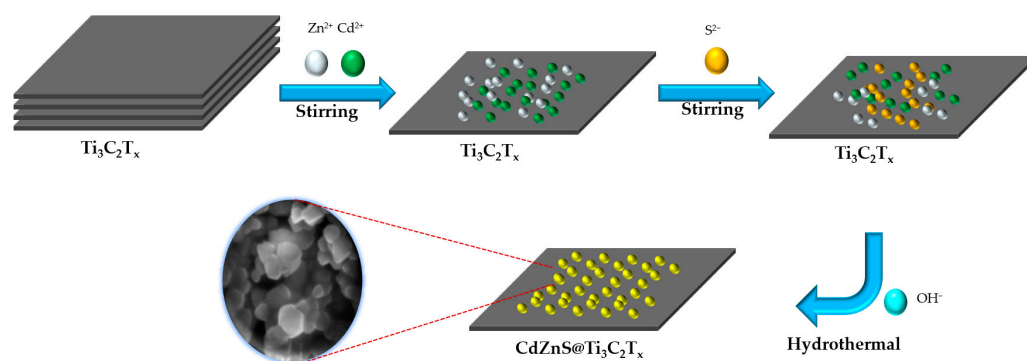


Figure 1. Schematic of synthesis of CdZnS/ $\text{Ti}_3\text{C}_2\text{T}_x$.

2.3. Characterization

The structure of the prepared photocatalyst was characterized by X-ray diffraction (XRD, PW3040/60, PANalytical, Almelo, The Netherlands) with a scanning range of $10\text{--}80^\circ$. The micromorphology, lattice stripe, and bonding information of the fabricated photocatalyst heterojunction interface were analyzed using field emission scanning electron microscopy (SEM, JSM-7001F, JEOL, Akishima, Japan) and field emission transmission electron microscopy (TEM, Talos-F200S, FEI, MA, USA). The valence bands and elemental compositions of the photocatalysts were investigated using X-ray photoelectron spectroscopy (XPS, K-Alpha Nexsa, Thermal Science, USA). The light absorption performance of the photocatalyst was analyzed with a UV-VIS spectrophotometer (UV-VIS, UV-3600Plus, Shimadzu, Japan) in the range of 200 to 800 nm. The photoluminescence intensity of

the samples at an excitation wavelength of 375 nm was determined using a fluorescence spectrometer (PL, FS5, Edinburgh Instruments, Livingston, UK).

2.4. Photoelectrochemical Measurement

Electrochemical impedance spectroscopy (EIS) and photocurrent response tests were performed using a standard three-electrode system at room temperature. A homogeneous suspension was formed by adding 10 mg of the sample to a mixture of 200 μ L ethanol and 20 μ L Nafion solution, followed by sonication for 30 min. The suspension was lowered onto the surface of cleaned tin fluoride oxide (FTO)-doped glass. Subsequently, the substrate was dried at 60 $^{\circ}$ C for 12 h. For recording photoresponse signals, a 300 W Xe lamp (with a UV cutoff filter, $\lambda > 420$ nm) was used as the light source. The frequency range of the electrochemical impedance spectroscopy (EIS) measurement was 10^5 Hz to 0.1 Hz.

2.5. Photocatalytic H_2 Evolution Performance

The photocatalytic hydrogen evolution reaction was conducted on an all-glass automated on-line trace gas analysis system (Labsolar-6A, PerfectLight, Beijing, China). A 10 mg quantity of photocatalyst was evenly dispersed in 100 mL of 0.35 M $Na_2S/0.25$ M sodium sulfite aqueous solution and stirred using sonication for 30 min. The 300 W Xe lamp is equipped with a 420 nm cutoff filter ($\lambda > 420$ nm). Before illumination, the system was evacuated to eliminate the influence of impurities, which were detected using a gas chromatograph (GC9790II, FuLi, Zhejiang, China. TCD detector, and Ar as the carrier gas). Hydrogen production per hour was recorded. The apparent quantum yield (AQY) was measured under similar photocatalytic conditions. The difference is that AQY was measured using a 420 nm bandpass filter and the optical power density was measured using an irradiator. AQY was calculated according to Equation (1) [45]:

$$AQY(\%) = \frac{(\text{number of evolved } H_2 \text{ molecules} * 2)}{(\text{number of incident photos})} \times 100\% \quad (1)$$

3. Results and Discussion

The XRD patterns of the as-prepared samples are shown in Figure 2. As can be seen, the CZS with an amphibolite structure had a distinct characteristic peak. According to the standard card, it can be indexed to the standard hexagonal phase cadmium sulfide (JCPDS 41-1049) and cubic phase zinc sulfide (JCPDS 05-0566). In contrast to them, half of the Cd atoms were replaced by Zn atoms, indicating the formation of a homogeneous solid-phase solution. It was not a mixture of cadmium sulfide and zinc sulfide on the physical layer. The peaks of the CZS/ $Ti_3C_2T_x$ composite photocatalyst at 26.5° , 44.8° , and 52.3° can be ascribed to the (111), (220), and (311) planes of CZS, respectively, which is consistent with the XRD peak positions of CZS in previous literature [28]. The diffraction peaks of $Ti_3C_2T_x$ were consistent with previous literature reports [46]. Compared to cubic zinc sulfide (JCPDS 05-0566), CZS exhibited the polyphase characteristics of the hexagonal phase, with a slight shift towards lower angles. This indicates that increasing the zinc content in the CZS solid solution transformed the crystal phase from hexagonal cadmium sulfide to cubic zinc sulfide, suggesting that the formed CZS was a solid solution rather than a physical mixture of cadmium sulfide and zinc sulfide. Compared with the original CZS, no significant shift was observed on the CZS/ $Ti_3C_2T_x$ composite photocatalyst, which indicates that the recombination of CZS and $Ti_3C_2T_x$ did not change the crystal orientation of CZS. The absence of $Ti_3C_2T_x$ in the diffraction pattern was mainly due to its low quantity and CZS covering the surface of $Ti_3C_2T_x$.

Scanning electron microscopy (SEM) and transmission electron microscopy (TEM) were used to analyze the morphology and microstructure of the samples. The SEM and TEM images of CZS and CZS-2 are shown in Figure 3. The samples were initially synthesized as agglomerated nanoparticles (Figure 3a,d). $Ti_3C_2T_x$ has a unique layered structure (Figure 3c). As shown in Figure 3b, it can be seen that the CZS-2 sample had a relatively

obvious structure of particles attached to the flake. CZS nanoparticles were covered on the flake $\text{Ti}_3\text{C}_2\text{T}_x$. Thus, the structure had a larger contact area and stronger photoadsorption capacity. Moreover, more light reflection and light scattering on the uneven surface of the hybrid layers also improved the utilization rate of light. In addition, the gap between the layers also facilitated the entry of the sacrifice agent. Figure 3e shows two different lattices, typically 0.24 nm corresponding to the (103) plane of $\text{Ti}_3\text{C}_2\text{T}_x$, and 0.32 nm corresponding to the (111) plane of CZS. The coexistence of these two lattices indicates the successful synthesis of the CZS/ $\text{Ti}_3\text{C}_2\text{T}_x$ heterojunction photocatalyst. The uniform distribution of C, S, Zn, Cd, and Ti elements on the energy dispersive X-ray spectroscopy (EDX) mappings indicates the uniform coverage of CZS nanoparticles on $\text{Ti}_3\text{C}_2\text{T}_x$ (shown in Figure 3f). The similarity of the molar ratios of each element (Figure 3g) to the experimental sample further verifies the successful preparation of the sample.

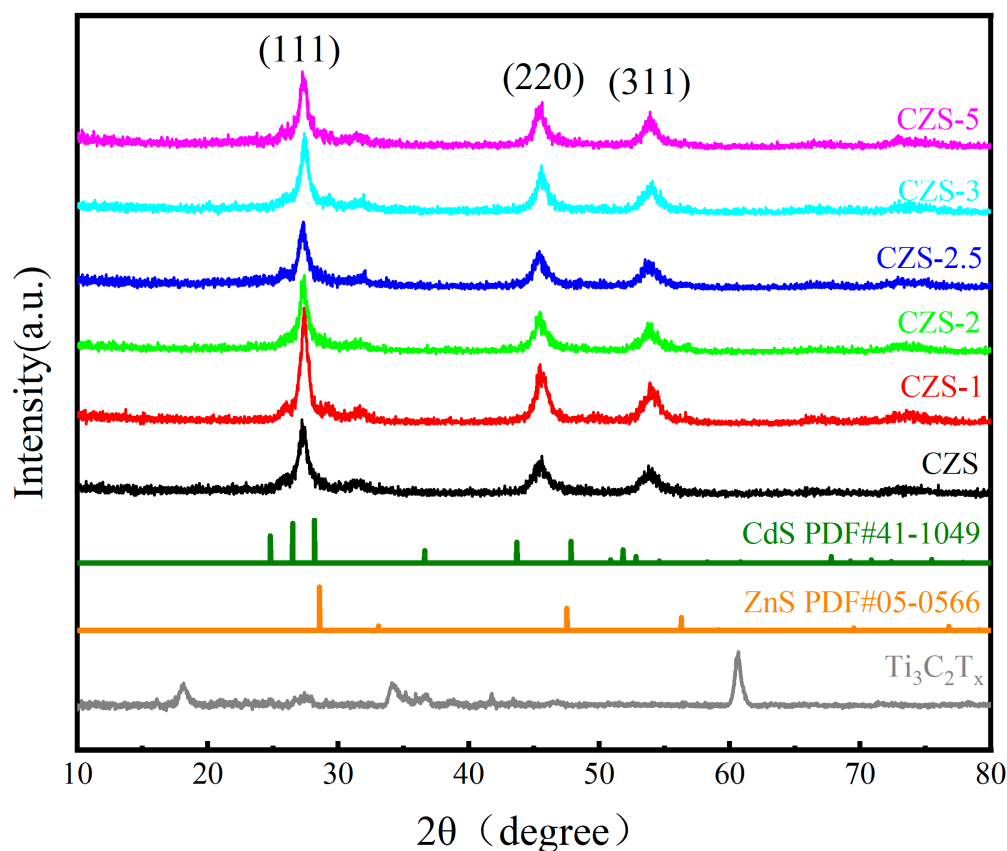


Figure 2. XRD patterns of as-prepared samples.

The surface composition and chemical valence of CZS-2 were analyzed by X-ray photoelectron spectroscopy (XPS). As shown in Figure 4a, S, Zn, Cd, C, and other elements could be detected on CZS-2. In comparison with the original CZS, slight shifts in the peaks of CZS-2 could be observed, indicating a strong interaction between $\text{Ti}_3\text{C}_2\text{T}_x$ and CZS. Due to its extremely low content (Figure 4b) of $\text{Ti}_3\text{C}_2\text{T}_x$ and coverage by CZS, no obvious peak could be detected on the full spectrum of the Ti element. The peaks at 454.9, 456.0, and 461.1 eV on the pristine $\text{Ti}_3\text{C}_2\text{T}_x$ corresponded to Ti-C, Ti-X, and Ti-O, respectively (Figure 4b). The C 1s of CZS-2 corresponded to the C-C, C-C-O, and C-F bonds at 284.8, 287.7, and 293.4 eV, respectively (Figure 4c). Two peaks of S 2p, at 162.0 and 168.8 eV, corresponded to S 2p_{3/2} and S 2p_{1/2} (Figure 4d), respectively. Two peaks of Cd 3d at 405.0 and 411.7 eV corresponded to Cd 3d_{5/2} and Cd 3d_{3/2} (Figure 4e), respectively. Two peaks of Zn 2p at 1044.5 and 1021.5 eV corresponded to Zn 2p_{3/2} and Zn 2p_{1/2} (Figure 4f), respectively. Compared with the standard electron binding energy control, there was a slight shift in the peak positions of these elements, mainly due to the strong interaction

between $\text{Ti}_3\text{C}_2\text{T}_x$ and CZS. The above results indicate the successful preparation of the CZS/ $\text{Ti}_3\text{C}_2\text{T}_x$ composite photocatalyst [47].

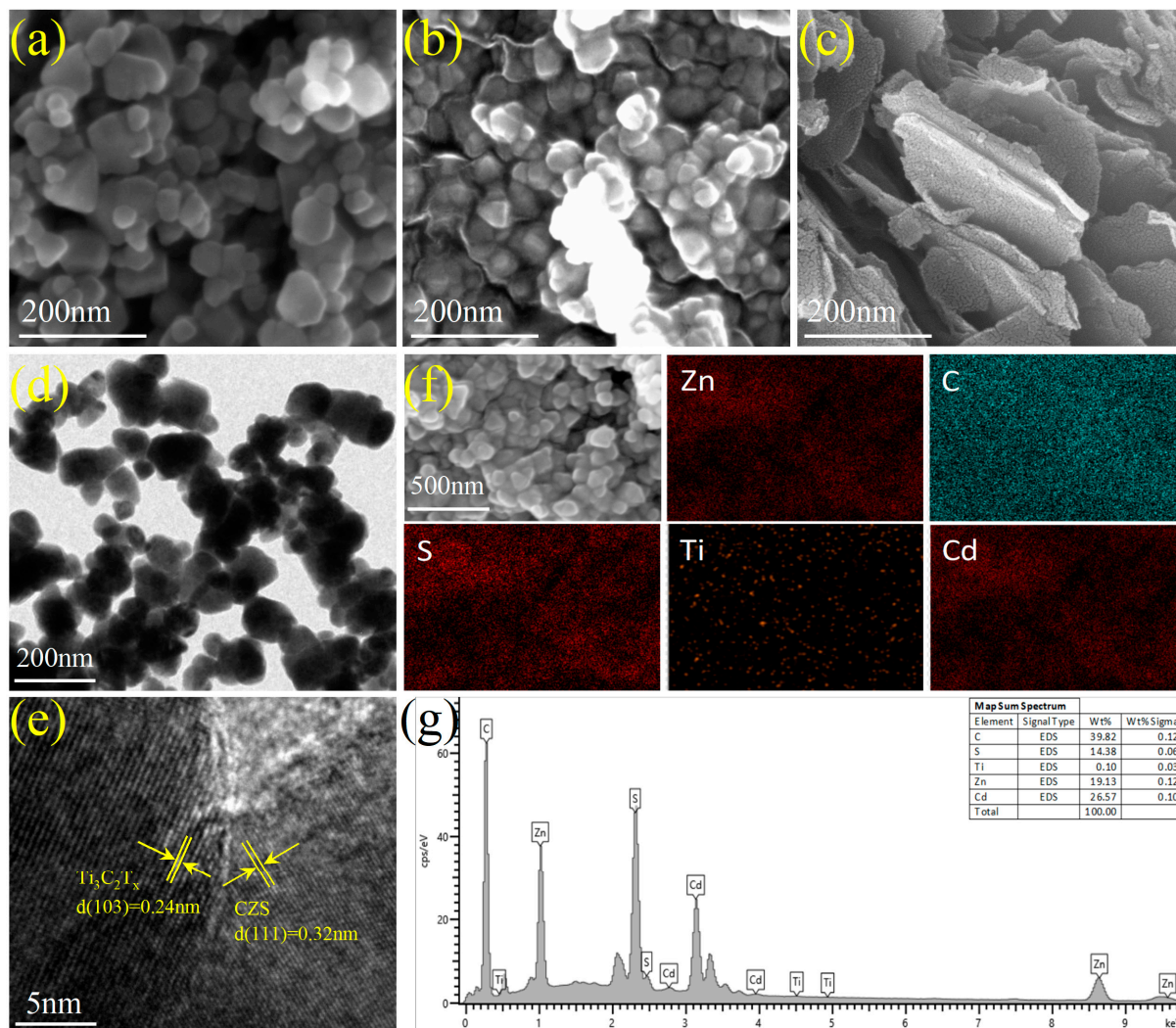


Figure 3. SEM images of (a) CZS, (b) CZS-2, and (c) $\text{Ti}_3\text{C}_2\text{T}_x$; TEM images of CZS-2 (d,e); EDS mappings of CZS-2 (f); EDX spectra of CZS-2 (g).

UV-VIS diffuse reflectance spectroscopy (DRS) is widely used to investigate optical absorption of photocatalysts. In order to explore effective activity of the CZS/ $\text{Ti}_3\text{C}_2\text{T}_x$ composite photocatalyst, DRS tests were performed in the range of 300–800 nm. As shown in Figure 5a, the CZS/ $\text{Ti}_3\text{C}_2\text{T}_x$ photocatalyst had good light absorption ability from 300 to 500 nm, and the absorption edge appeared at about 480 nm. With increasing the amount of $\text{Ti}_3\text{C}_2\text{T}_x$, the light absorption gradually increased after 480 nm. In order to further study the band structure, the Kubelka–Munk equation [48] was used to calculate the band gap:

$$\alpha h\nu = A(h\nu - E_g)^{1/2} \quad (2)$$

Here α , $h\nu$, and A denote the absorption coefficient, photon energy, and a constant, respectively. The calculated band gap values of CZS and CZS-2 in the original sample were 2.572 eV and 2.583 eV (Figure 5b), respectively, which also verified that CZS-2 had stronger light absorption ability. The valence band (VB) spectrum of XPS (shown in Figure 5c,d) was used to further analyze the band structure. The results show that the band gap and valence band of CZS were 2.572 eV and 1.55 eV, respectively, and the band gap and valence band of CZS-2 were 2.583 eV and 1.48 eV, respectively. The conduction band

(CB) of CZS was -1.022 eV; the CB of CZS-2 was -1.103 eV according to the formula $E_{VB} = E_{CB} + E_g$. Compared to CZS, CZS-2 had a more negative CB potential, which enhanced its photocatalytic reduction ability and was more conducive to the photocatalytic decomposition of the hydrogen water solution.

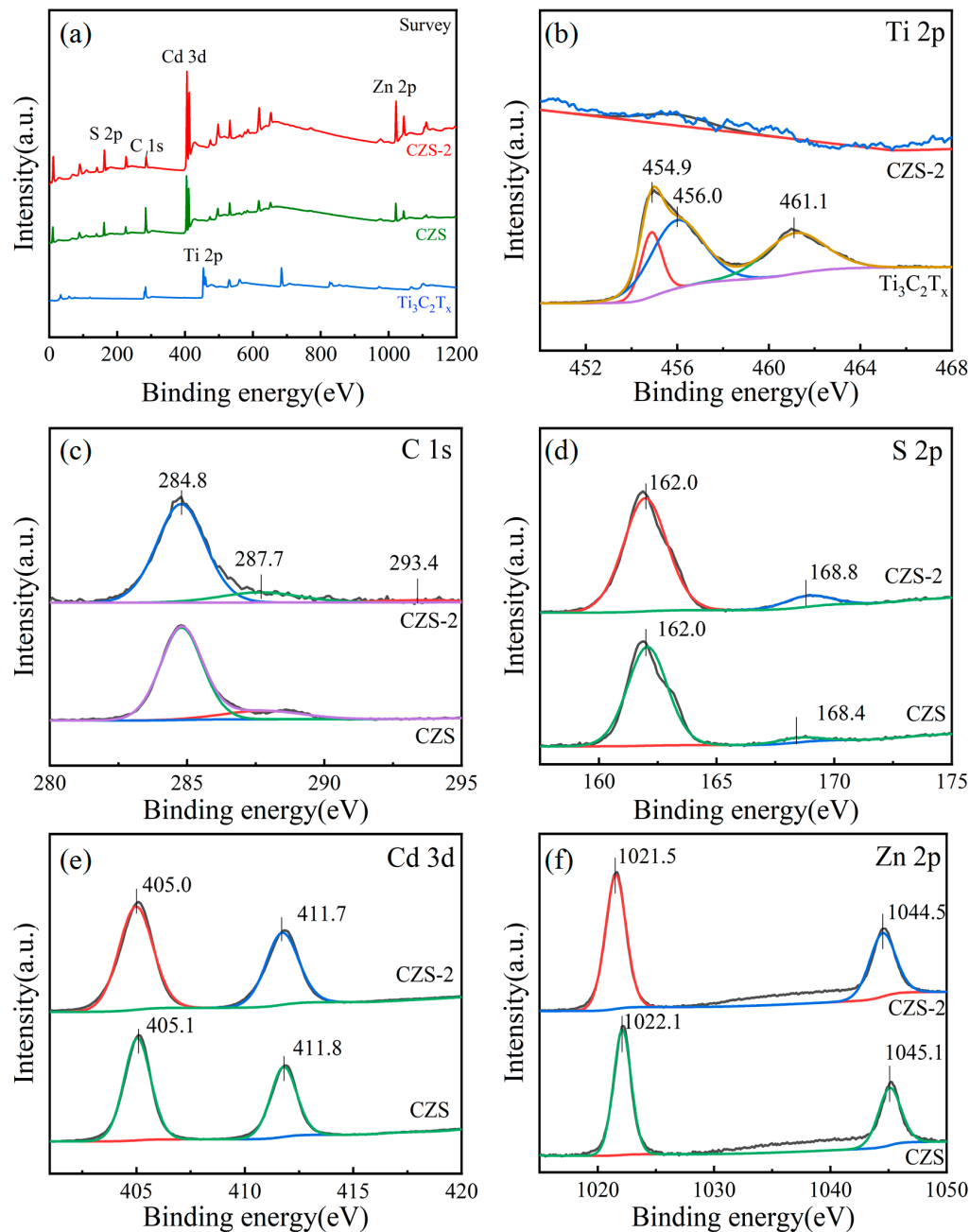


Figure 4. XPS spectrum of CZS, CZS-2, and $Ti_3C_2T_x$; (a) survey, (b) Ti 2p, (c) C 1s, (d) S 2p, (e) Cd 3d, (f) Zn 2p.

In order to further investigate the effect of $Ti_3C_2T_x$ on the charge transfer efficiency of CZS, the photocurrent response and photoluminescence maps were studied. As can be seen from Figure 6a, the photocurrent density of the CZS-2 composite photocatalyst was significantly higher than that of the original CZS sample, indicating that CZS had an improved photocurrent response and higher electron transfer efficiency after being combined with $Ti_3C_2T_x$ [49–51]. In Figure 6b, the PL emission intensity of the CZS-2 composite photocatalyst was also significantly lower than that of the original CZS. The

lower emission intensity reflects the lower binding rate of the photoelectron-hole pair, which means that the combination of the photoelectron-hole pair could be inhibited after recombination, and the photogenerated carrier separation efficiency was higher [52,53]. This phenomenon is consistent with the photocurrent response diagram.

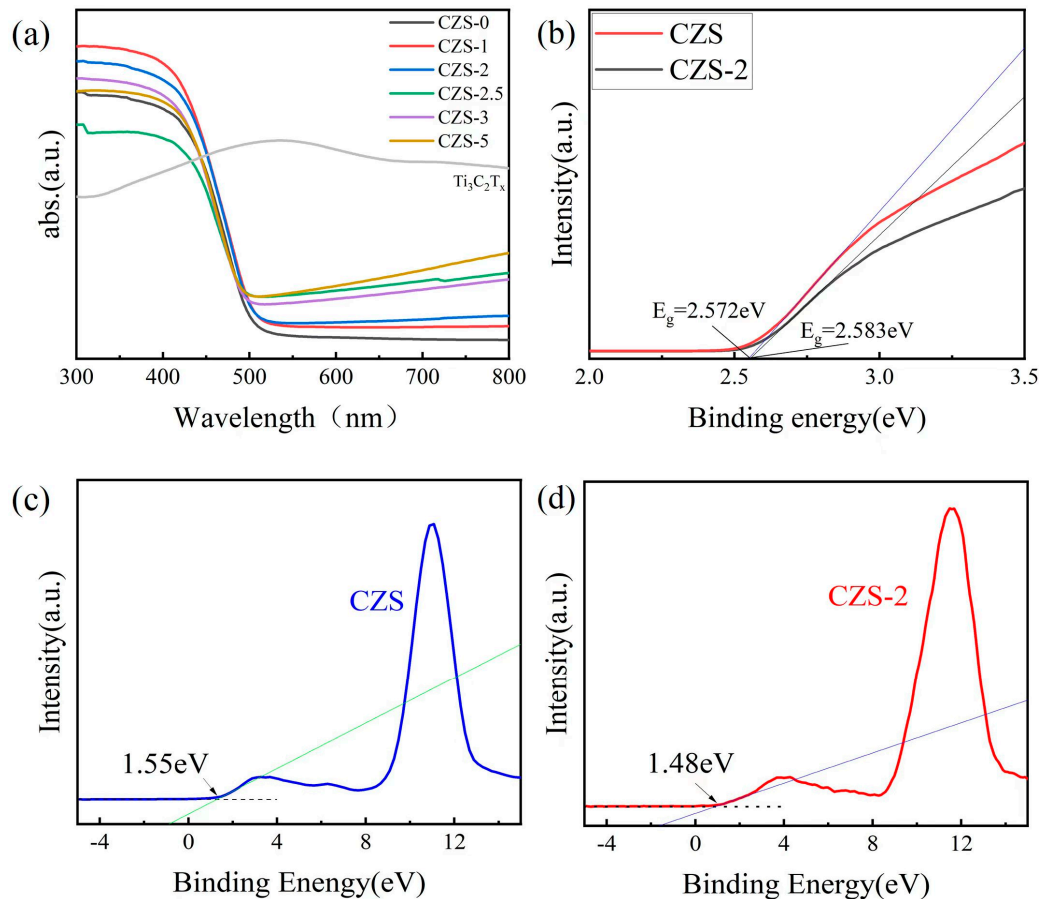


Figure 5. (a) UV-VIS DRS spectra of as-prepared samples; (b) Tauc plot of CZS and CZS-2. Valence band XPS spectra of (c) CZS and (d) CZS-2.

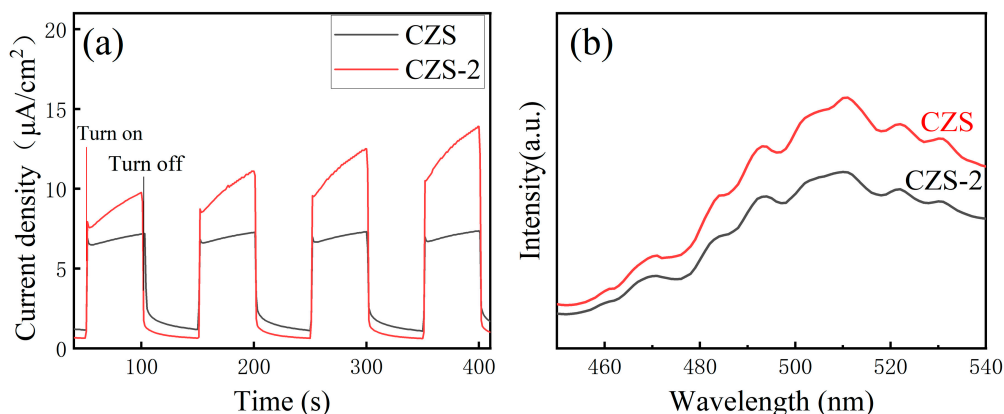


Figure 6. Excited state electron radioactive decay spectra (a), and transient photocurrent response of CZS and CZS-2 samples (b).

Under conditions of visible illumination (UV cut-off filter, $\lambda > 420$ nm), the hydrogen evolution performance of the CZS/ $\text{Ti}_3\text{C}_2\text{T}_x$ composite photocatalyst was analyzed. As shown in Figure 7a, CZS with different Mxene mass ratios had good stability in the hydrogen production process for 3 h. The hydrogen production performances of CZS/ $\text{Ti}_3\text{C}_2\text{T}_x$

showed an obvious upward trend with increasing the amount of $\text{Ti}_3\text{C}_2\text{T}_x$ in the solution using sodium sulfide and sodium sulfite as sacrificial agents. When the content of $\text{Ti}_3\text{C}_2\text{T}_x$ reached 2%, the hydrogen production performance reached a maximum value of $47.1 \text{ mmol g}^{-1} \text{ h}^{-1}$, which was 1.3 times that of the original CZS sample (Figure 7b). At 420 nm, it had a higher AQY value of 27.24%. Subsequently, with increasing the amount of $\text{Ti}_3\text{C}_2\text{T}_x$, the hydrogen production performance gradually decreased, indicating that excessive addition of $\text{Ti}_3\text{C}_2\text{T}_x$ may have a negative impact on the photocatalytic activity of CZS. An excessive amount of $\text{Ti}_3\text{C}_2\text{T}_x$ can result in a decrease in the concentration of the main photocatalyst CZS and also hinder the penetration of light, thereby impeding the utilization efficiency of CZS for light. Therefore, the optimum loading for $\text{Ti}_3\text{C}_2\text{T}_x$ is 2 wt.%. The hydrogen evolution stability of CZS/ $\text{Ti}_3\text{C}_2\text{T}_x$ was analyzed by four repeated experiments. After four cycles of 3 h (as shown in Figure 7c), the hydrogen evolution performance of CZS/ $\text{Ti}_3\text{C}_2\text{T}_x$ decreased slightly and the hydrogen production efficiency was 82.7%, as compared with that of the first cycle due to part of the photocatalyst covering the surface of the reaction vessel with hydrogen production, thus affecting the incident photon quantity.

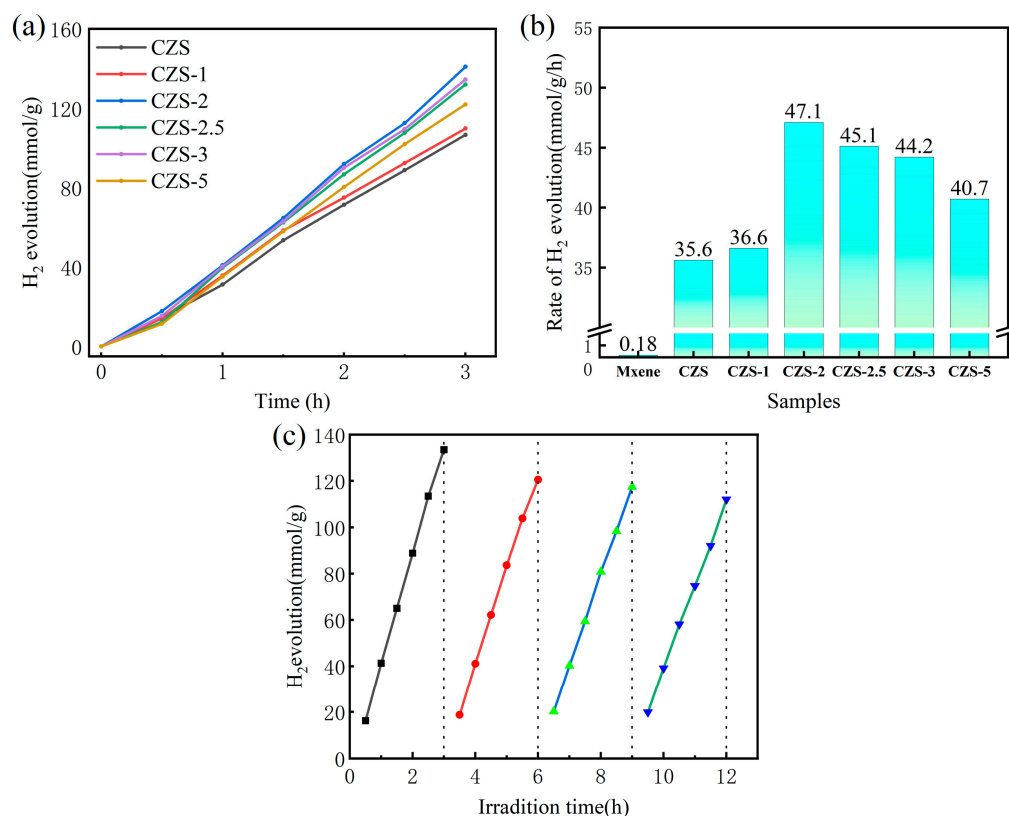


Figure 7. (a) The stability of hydrogen production performance of CZS with different Mxene mass ratios; (b) the rate of H_2 evolution of CZS and CZS- x ($x = 1, 2, 2.5, 3, 5$) under visible light irradiation; (c) photocatalytic hydrogen production stability test of CZS-2 during 12 h.

Figure 8 shows the possible photocatalytic hydrogen evolution mechanism in the CZS/ $\text{Ti}_3\text{C}_2\text{T}_x$ system. For the primitive CZS, when exposed to visible light ($\lambda > 420 \text{ nm}$) after excitation, the photogenerated electrons on VB were induced to transfer to CB, then combine with H^+ in water to produce hydrogen. The holes generated by the transfer of electrons on VB reacted with the sacrificial agents S^{2-} and SO_3^{2-} on the surface of the photocatalyst. In the absence of $\text{Ti}_3\text{C}_2\text{T}_x$ recombination, the photolithogenic holes and electrons showed a high and rapid recombination rate. After adding the appropriate quantity of $\text{Ti}_3\text{C}_2\text{T}_x$, a heterojunction could be formed. The Schottky barrier was generated on the CZS/ $\text{Ti}_3\text{C}_2\text{T}_x$ interface. Additionally, due to the higher Fermi energy level of $\text{Ti}_3\text{C}_2\text{T}_x$

compared to CZS, photogenerated electrons tended to migrate from the conduction band of CZS to $\text{Ti}_3\text{C}_2\text{T}_x$, effectively impeding the recombination of photogenerated electron-hole pairs and thereby enhancing the separation efficiency of electron-hole pairs. In addition, owing to the large dispersion area of Mxene, the agglomeration of CdZnS nanoparticles could be effectively inhibited. As a result, with the aid of $\text{Ti}_3\text{C}_2\text{T}_x$ Mxene, CZS showed an improved visible-light-driven photocatalytic hydrogen evolution.

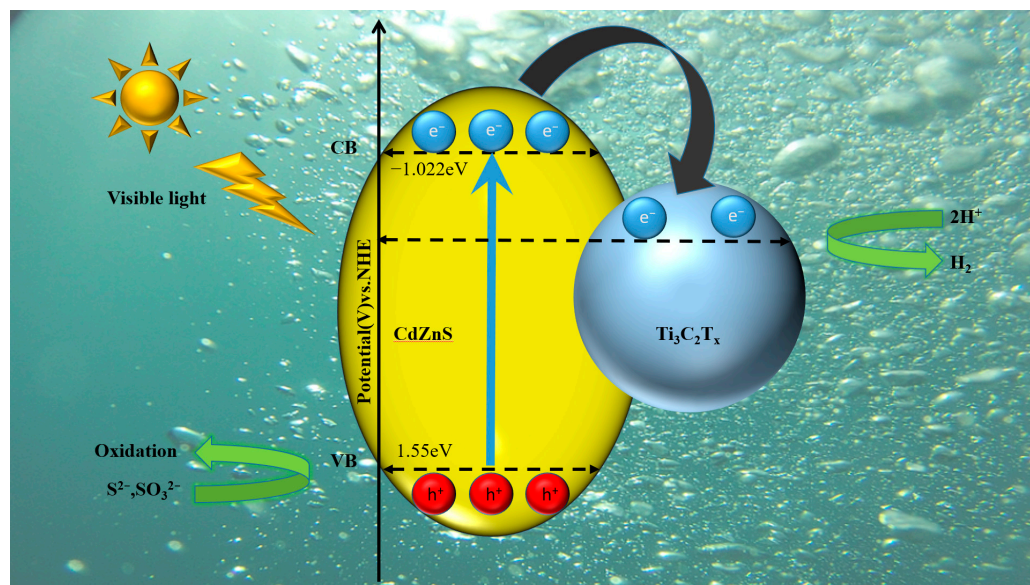


Figure 8. The possible photocatalytic hydrogen evolution mechanism in CdZnS/ $\text{Ti}_3\text{C}_2\text{T}_x$ system.

4. Conclusions

In summary, we have constructed and characterized an efficient photocatalyst of CZS nanoparticles overlaid on cocatalyst $\text{Ti}_3\text{C}_2\text{T}_x$ nanosheets using an in situ growth method. The photocatalytic hydrogen production performance of CZS can be effectively improved by adding an appropriate amount of $\text{Ti}_3\text{C}_2\text{T}_x$ (2% mass ratio), which can construct heterojunctions to block the recombination of electrons and holes induced by photogeneration. Under visible light irradiation, it reached a high photocatalytic hydrogen production value of $47.1 \text{ mmol g}^{-1} \text{ h}^{-1}$. It could also maintain a relatively stable hydrogen production over a long period of catalysis. The main reason for the success of the modification is that the Schottky barrier is conducive to the diffusion of electrons and inhibits the recombination of electron-hole pairs induced by photogeneration. At the same time, the zinc cadmium sulfide nanoparticles uniformly covered the $\text{Ti}_3\text{C}_2\text{T}_x$ nanosheets, also improving the utilization rate of light and relieving the agglomeration effect of the particles, thereby achieving a high hydrogen production performance. This work can provide some valuable guidance and ideas for selecting cocatalyst modification of CZS to improve the separation of electron-hole pairs and inhibit the recombination of electron-hole pairs.

Author Contributions: Investigation, methodology, data curation, Z.L. and Y.Z.; Visualization, X.Z. and Y.T.; writing—original draft preparation, Z.L.; writing—review and editing, Z.F., H.J. and Q.D.; conceptualization, Q.D.; supervision, S.Z. and Q.D.; funding acquisition, L.Y. and Q.D. All authors have read and agreed to the published version of the manuscript.

Funding: This research was funded by the National Natural Science Foundation of China (No. 22109032), the Guangzhou Science and Technology Plan Project (No. 202201010327), the Talent Cultivation Project of Guangzhou University (No. RP2021038), the Guangzhou Basic Research Program, City & University (Institute) Joint Funding Project (No. SL2022A03J01003) and Key Discipline of Materials Science and Engineering, Bureau of Education of Guangzhou (Grant number: 202255464).

Data Availability Statement: Not applicable.

Conflicts of Interest: The authors declare no conflict of interest.

References

1. Wu, X.; Luo, N.; Xie, S.; Zhang, H.; Zhang, Q.; Wang, F.; Wang, Y. Photocatalytic transformations of lignocellulosic biomass into chemicals. *Chem. Soc. Rev.* **2020**, *49*, 6198–6223. [[CrossRef](#)]
2. Wang, L.; Jin, P.X.; Huang, J.W.; She, H.D.; Wang, Q.Z. Integration of Copper(II)-Porphyrin Zirconium Metal-Organic Framework and Titanium Dioxide to Construct Z-Scheme System for Highly Improved Photocatalytic CO₂ Reduction. *Acs Sustain. Chem. Eng.* **2019**, *7*, 15660–15670. [[CrossRef](#)]
3. Hou, T.; Chen, H.; Li, Y.; Wang, H.; Yu, F.; Li, C.; Lin, H.; Li, S.; Wang, L. Unique Cd_{0.5}Zn_{0.5}S/WO_{3-x} direct Z-scheme heterojunction with S, O vacancies and twinning superlattices for efficient photocatalytic water-splitting. *Dalton Trans.* **2022**, *51*, 1150–1162. [[CrossRef](#)] [[PubMed](#)]
4. Lee, H.J.; Jin, Y.; Park, S.S.; Soo, H.S.; Lee, G.D. Photocatalytic Degradation of Rhodamine B Using Cd_{0.5}Zn_{0.5}S/ZnO Photocatalysts under Visible Light Irradiation. *Appl. Chem. Eng.* **2015**, *26*, 356–361. [[CrossRef](#)]
5. Liang, Q.; Jin, J.; Liu, C.; Xu, S.; Yao, C.; Li, Z. Fabrication of the ternary heterojunction Cd_{0.5}Zn_{0.5}S@UIO-66@g-C₃N₄ for enhanced visible-light photocatalytic hydrogen evolution and degradation of organic pollutants. *Inorg. Chem. Front.* **2018**, *5*, 335–343. [[CrossRef](#)]
6. Mu, P.; Zhou, M.; Yang, K.; Zhou, C.; Mi, Y.; Yu, Z.; Lu, K.; Li, Z.; Ouyang, S.; Huang, W.; et al. Sulfur vacancies engineered over Cd_{0.5}Zn_{0.5}S by Yb³⁺/Er³⁺ co-doping for enhancing photocatalytic hydrogen evolution. *Sustain. Energy Fuels* **2021**, *5*, 5814–5824. [[CrossRef](#)]
7. Xiao, L.; Su, T.; Wang, Z.; Zhang, K.; Peng, X.; Han, Y.; Li, Q.; Wang, X. Enhanced Photocatalytic Hydrogen Evolution by Loading Cd_{0.5}Zn_{0.5}S QDs onto Ni₂P Porous Nanosheets. *Nanoscale Res. Lett.* **2018**, *13*, 1–9. [[CrossRef](#)]
8. Zeng, C.; Hu, Y.; Zhang, T.; Dong, F.; Zhang, Y.; Huang, H. A core-satellite structured Z-scheme catalyst Cd_{0.5}Zn_{0.5}S/BiVO₄ for highly efficient and stable photocatalytic water splitting. *J. Mater. Chem. A* **2018**, *6*, 16932–16942. [[CrossRef](#)]
9. Fujishima, A.; Honda, K. Electrochemical photolysis of water at a semiconductor electrode. *Nature* **1972**, *238*, 37–38. [[CrossRef](#)]
10. Poudel, M.B.; Kim, A.R.; Ramakrishnan, S.; Logeshwaran, N.; Ramasamy, S.K.; Kim, H.J.; Yoo, D.J. Integrating the essence of metal organic framework-derived ZnCoTe-N-C/MoS₂ cathode and ZnCo-NPS-N-CNT as anode for high-energy density hybrid supercapacitors. *Compos. Part. B Eng.* **2022**, *247*, 110339. [[CrossRef](#)]
11. Poudel, M.B.; Kim, A.A.; Lohani, P.C.; Yoo, D.J.; Kim, H.J. Assembling zinc cobalt hydroxide/ternary sulfides heterostructure and iron oxide nanorods on three-dimensional hollow porous carbon nanofiber as high energy density hybrid supercapacitor. *J. Energy Storage* **2023**, *60*, 106713. [[CrossRef](#)]
12. Poudel, M.B.; Lohani, P.C.; Acharya, D.; Kandel, D.R.; Kim, A.A.; Yoo, D.J. MOF derived hierarchical ZnNiCo-LDH on vapor solid phase grown Cu_xO nanowire array as high energy density asymmetric supercapacitors. *J. Energy Storage* **2023**, *72*, 108220. [[CrossRef](#)]
13. Mamiyev, Z.; Balayeva, N.O. Metal Sulfide Photocatalysts for Hydrogen Generation: A Review of Recent Advances. *Catalysts* **2022**, *12*, 1316. [[CrossRef](#)]
14. Ganapathy, M.; Chang, C.T.; Alagan, V. Facile preparation of amorphous SrTiO₃– crystalline PbS heterojunction for efficient photocatalytic hydrogen production. *Int. J. Hydrog. Energy* **2022**, *47*, 27555–27565. [[CrossRef](#)]
15. Zhuge, K.; Chen, Z.; Yang, Y.; Wang, J.; Shi, Y.; Li, Z. In-situ photodeposition of MoS₂ onto CdS quantum dots for efficient photocatalytic H₂ evolution. *Appl. Surf. Sci.* **2021**, *539*, 148243. [[CrossRef](#)]
16. Zhu, Q.H.; Xu, Q.; Du, M.M.; Zeng, X.F.; Zhong, G.F.; Qiu, B.C.; Zhang, J.L. Recent Progress of Metal Sulfide Photocatalysts for Solar Energy Conversion. *Adv. Mater.* **2022**, *34*, e2202929. [[CrossRef](#)]
17. Poudel, M.B.; Awasthi, G.P.; Kim, H.J. Novel insight into the adsorption of Cr(VI) and Pb(II) ions by MOF derived Co-Al layered double hydroxide @hematite nanorods on 3D porous carbon nanofiber network. *Chem. Eng. J.* **2021**, *417*, 129312. [[CrossRef](#)]
18. Ji, Q.; Xu, J.; Wang, C.; Wang, L. Controlling the coordination environment of Co atoms derived from Co/ZIF-8 for boosting photocatalytic H₂ evolution of CdS. *J. Colloid. Interface Sci.* **2021**, *596*, 139–147. [[CrossRef](#)]
19. Qin, X.; Cao, R.; Gong, W.; Luo, L.; Shi, G.; Ji, L.; Zhu, A. Hydrothermal growth of ZnCdS/TiO₂ nanoparticles on the surface of Ti₃C₂ MXene sheet to enhance photocatalytic performance under visible light. *J. Solid. State Chem.* **2022**, *306*, 122751. [[CrossRef](#)]
20. Jin, S.; Jing, H.; Wang, L.; Hu, Q.; Zhou, A. Construction and performance of CdS/MoO₂@Mo₂C-MXene photocatalyst for H₂ production. *J. Adv. Ceram.* **2022**, *11*, 1431–1444. [[CrossRef](#)]
21. Cao, B.; Wan, S.; Wang, Y.; Guo, H.; Ou, M.; Zhong, Q. Highly-efficient visible-light-driven photocatalytic H₂ evolution integrated with microplastic degradation over MXene/Zn_xCd_{1-x}S photocatalyst. *J. Colloid. Interface Sci.* **2022**, *605*, 311–319. [[CrossRef](#)] [[PubMed](#)]
22. Zhou, L.; Dong, Y. Influence of the reaction temperature on Cd_{1-x}Zn_xS thin films with chemical bath deposited. In Proceedings of the 12th China International Nanoscience and Technology Symposium, Chengdu and the Nano-Products Exposition, Chengdu, China, 27–31 October 2014; pp. 52–56.
23. Chen, Y.; Guo, L. Highly efficient visible-light-driven photocatalytic hydrogen production from water using Cd_{0.5}Zn_{0.5}S/TNTs (titanate nanotubes) nanocomposites without noble metals. *J. Mater. Chem.* **2012**, *22*, 7507–7514. [[CrossRef](#)]

24. Yu, K.; Huang, H.-B.; Zeng, X.-Y.; Xu, J.-Y.; Yu, X.-T.; Liu, H.-X.; Cao, H.-L.; Lu, J.; Cao, R. CdZnS nanorods with rich sulphur vacancies for highly efficient photocatalytic hydrogen production. *Chem. Commun.* **2020**, *56*, 7765–7768. [[CrossRef](#)] [[PubMed](#)]
25. Zhang, K.; Dai, Y.; Zhou, Z.; Jan, S.U.; Guo, L.; Gong, J.R. Polarization-induced saw-tooth-like potential distribution in zinblendewurtzite superlattice for efficient charge separation. *Nano Energy* **2017**, *41*, 101–108. [[CrossRef](#)]
26. Chen, D.; Xu, Y.; Zhang, Y.; Sheng, W.; Qian, G. Nickel hydroxide as a non-noble metal co-catalyst decorated on Cd_{0.5}Zn_{0.5}S solid solution for enhanced hydrogen evolution. *Rsc Adv.* **2021**, *11*, 20479–20485. [[CrossRef](#)] [[PubMed](#)]
27. Yin, Q.; Cao, Z.; Wang, Z.; Zhai, J.; Li, M.; Guan, L.; Fan, B.; Liu, W.; Shao, G.; Xu, H.; et al. Z-scheme TiO₂@Ti₃C₂/Cd_{0.5}Zn_{0.5}S nanocomposites with efficient photocatalytic performance via one-step hydrothermal route. *Nanotechnology* **2021**, *32*, 015706. [[CrossRef](#)]
28. Tao, J.; Wang, M.; Liu, G.; Liu, Q.; Lu, L.; Wan, N.; Tang, H.; Qiao, G. Efficient photocatalytic hydrogen evolution coupled with benzaldehyde production over 0D Cd_{0.5}Zn_{0.5}S/2D Ti₃C₂ Schottky heterojunction. *J. Adv. Ceram.* **2022**, *11*, 1117–1130. [[CrossRef](#)]
29. Sherryrna, A.; Tahir, M. Role of surface morphology and terminating groups in titanium carbide MXenes (Ti₃C₂T_x) cocatalysts with engineering aspects for modulating solar hydrogen production: A critical review. *Chem. Eng. J.* **2022**, *433*, 134573. [[CrossRef](#)]
30. Liu, X.; Zhao, Y.; Yang, X.; Liu, Q.; Yu, X.; Li, Y.; Tang, H.; Zhang, T. Porous Ni₅P₄ as a promising cocatalyst for boosting the photocatalytic hydrogen evolution reaction performance. *Appl. Catal. B Environ.* **2020**, *275*, 119144. [[CrossRef](#)]
31. Shao, Y.; Feng, K.; Guo, J.; Zhang, R.; He, S.; Wei, X.; Lin, Y.; Ye, Z.; Chen, K. Electronic structure and enhanced photoelectrocatalytic performance of Ru_xZn_{1-x}O/Ti electrodes. *J. Adv. Ceram.* **2021**, *10*, 1025–1041. [[CrossRef](#)]
32. Ganguly, P.; Harb, M.; Cao, Z.; Cavallo, L.; Breen, A.; Dervin, S.; Dionysiou, D.D.; Pillai, S.C. 2D Nanomaterials for Photocatalytic Hydrogen Production. *Acs Energy Lett.* **2019**, *4*, 1687–1709. [[CrossRef](#)]
33. Wang, W.; Chen, H.; Wu, J.; Wang, H.; Li, S.; Wang, B.; Li, Y.; Lin, H.; Wang, L. Unique hollow heterostructured CdS/Cd_{0.5}Zn_{0.5}S-Mo_{1-x}W_xS₂: Highly-improved visible-light-driven H₂ generation via synergy of Cd_{0.5}Zn_{0.5}S protective shell and defect-rich Mo_{1-x}W_xS₂ cocatalyst. *Nano Res.* **2022**, *15*, 985–995. [[CrossRef](#)]
34. Zuo, G.; Wang, Y.; Teo, W.L.; Xie, A.; Guo, Y.; Dai, Y.; Zhou, W.; Jana, D.; Xian, Q.; Dong, W.; et al. Ultrathin ZnIn₂S₄ Nanosheets Anchored on Ti₃C₂T_x MXene for Photocatalytic H₂ Evolution. *Angew. Chem. Int. Ed.* **2020**, *59*, 11287–11292. [[CrossRef](#)] [[PubMed](#)]
35. Zhong, T.; Yu, Z.; Jiang, R.; Hou, Y.; Chen, H.; Ding, L.; Lian, C.; Zou, B. Surface-Activated Ti₃C₂T_x MXene Cocatalyst Assembled with CdZnS-Formed 0D/2D CdZnS/Ti₃C₂-A(40) Schottky Heterojunction for Enhanced Photocatalytic Hydrogen Evolution. *Sol. Rrl* **2022**, *6*, 2100863. [[CrossRef](#)]
36. Shi, X.; Wang, P.; Lan, L.; Jia, S.; Wei, Z. Construction of BiOBr_xI_{1-x}/MXene Ti₃C₂T_x composite for improved photocatalytic degradability. *J. Mater. Sci. Mater. Electron.* **2019**, *30*, 19804–19812. [[CrossRef](#)]
37. Chen, Y.; Yin, X.; Lei, S.; Dai, X.; Xu, X.; Shi, W.; Liu, W.; Wu, F.; Cao, X. MXene for aqueous zinc-based energy storage devices. *Funct. Mater. Lett.* **2021**, *14*, 2130011. [[CrossRef](#)]
38. Luo, H.; Liu, B.; Yang, Z.; Wan, Y.; Zhong, C. The Trade-Offs in the Design of Reversible Zinc Anodes for Secondary Alkaline Batteries. *Electrochem. Energy Rev.* **2022**, *5*, 187–210. [[CrossRef](#)]
39. Lu, W.; Zhang, C.; Zhang, H.; Li, X. Anode for Zinc-Based Batteries: Challenges, Strategies, and Prospects. *Acs Energy Lett.* **2021**, *6*, 2765–2785. [[CrossRef](#)]
40. Chen, X.; Guo, Y.; Bian, R.; Ji, Y.; Wang, X.; Zhang, X.; Cui, H.; Tian, J. Titanium carbide MXenes coupled with cadmium sulfide nanosheets as two-dimensional/two-dimensional heterostructures for photocatalytic hydrogen production. *J. Colloid. Interface Sci.* **2022**, *613*, 644–651. [[CrossRef](#)]
41. Liu, Q.Q.; Huang, J.X.; Tang, H.; Yu, X.H.; Shen, J. Construction 0D TiO₂ nanoparticles/2D CoP nanosheets heterojunctions for enhanced photocatalytic H₂ evolution activity. *J. Mater. Sci. Technol.* **2020**, *56*, 196–205. [[CrossRef](#)]
42. Handoko, A.D.; Fredrickson, K.D.; Anasori, B.; Convey, K.W.; Johnson, L.R.; Gogotsi, Y.; Vojvodic, A.; Seh, Z.W. Tuning the Basal Plane Functionalization of Two-Dimensional Metal Carbides (MXenes) to Control Hydrogen Evolution Activity. *Acs Appl. Energy Mater.* **2018**, *1*, 173–180. [[CrossRef](#)]
43. Seh, Z.W.; Fredrickson, K.D.; Anasori, B.; Kibsgaard, J.; Strickler, A.L.; Lukatskaya, M.R.; Gogotsi, Y.; Jaramillo, T.F.; Vojvodic, A. Two-Dimensional Molybdenum Carbide (MXene) as an Efficient Electrocatalyst for Hydrogen Evolution. *Acs Energy Lett.* **2016**, *1*, 589–594. [[CrossRef](#)]
44. Cai, T.; Wang, L.; Liu, Y.; Zhang, S.; Dong, W.; Chen, H.; Yi, X.; Yuan, J.; Xia, X.; Liu, C.; et al. Ag₃PO₄/Ti₃C₂ MXene interface materials as a Schottky catalyst with enhanced photocatalytic activities and anti-photocorrosion performance. *Appl. Catal. B Environ.* **2018**, *239*, 545–554. [[CrossRef](#)]
45. Qureshi, M.; Takanabe, K. Insights on Measuring and Reporting Heterogeneous Photocatalysis: Efficiency Definitions and Setup Examples. *Chem. Mater.* **2017**, *29*, 158–167. [[CrossRef](#)]
46. Wang, H.; Wu, Y.; Xiao, T.; Yuan, X.; Zeng, G.; Tu, W.; Wu, S.; Lee, H.Y.; Tan, Y.Z.; Chew, J.W. Formation of quasi-core-shell In₂S₃/anatase TiO₂@metallic Ti₃C₂T_x hybrids with favorable charge transfer channels for excellent visible-light-photocatalytic performance. *Appl. Catal. B Environ.* **2018**, *233*, 213–225. [[CrossRef](#)]
47. Ismael, M.; Elhaddad, E.; Wark, M. Construction of SnO₂/g-C₃N₄ composite photocatalyst with enhanced interfacial charge separation and high efficiency for hydrogen production and Rhodamine B degradation. *Colloids Surf. A Physicochem. Eng. Asp.* **2022**, *638*, 128288. [[CrossRef](#)]
48. Kokhanovsky, A.A. Physical interpretation and accuracy of the Kubelka-Munk theory. *J. Phys. D Appl. Phys.* **2007**, *40*, 2210–2216. [[CrossRef](#)]

49. Liu, Y.; Li, Y.-H.; Li, X.; Zhang, Q.; Yu, H.; Peng, X.; Peng, F. Regulating Electron-Hole Separation to Promote Photocatalytic H₂ Evolution Activity of Nanoconfined Ru/MXene/TiO₂ Catalysts. *Acs Nano* **2020**, *14*, 14181–14189. [[CrossRef](#)]
50. Wang, H.; Sun, Y.; Wu, Y.; Tu, W.; Wu, S.; Yuan, X.; Zeng, G.; Xu, Z.J.; Li, S.; Chew, J.W. Electrical promotion of spatially photoinduced charge separation via interfacial-built-in quasi-alloying effect in hierarchical Zn₂In₂S₅/Ti₃C₂(OH)_xhybrids toward efficient photocatalytic hydrogen evolution and environmental remediation. *Appl. Catal. B Environ.* **2019**, *245*, 290–301. [[CrossRef](#)]
51. Peng, C.; Yang, X.; Li, Y.; Yu, H.; Wang, H.; Peng, F. Hybrids of Two-Dimensional Ti₃C₂ and TiO₂ Exposing {001} Facets toward Enhanced Photocatalytic Activity. *Acs Appl. Mater. Interfaces* **2016**, *8*, 6051–6060. [[CrossRef](#)]
52. Ismael, M. Highly effective ruthenium-doped TiO₂ nanoparticles photocatalyst for visible-light-driven photocatalytic hydrogen production. *New J. Chem.* **2019**, *43*, 9596–9605. [[CrossRef](#)]
53. Low, J.; Zhang, L.; Tong, T.; Shen, B.; Yu, J. TiO₂/MXene Ti₃C₂ composite with excellent photocatalytic CO₂ reduction activity. *J. Catal.* **2018**, *361*, 255–266. [[CrossRef](#)]

Disclaimer/Publisher's Note: The statements, opinions and data contained in all publications are solely those of the individual author(s) and contributor(s) and not of MDPI and/or the editor(s). MDPI and/or the editor(s) disclaim responsibility for any injury to people or property resulting from any ideas, methods, instructions or products referred to in the content.